Conformally Decambered Natural Laminar Flow Blades for Vertical Axis Wind Turbines

Idan Arava

Faculty of Mechanical Engineering, Technion – Israel Institute of Technology

Technion City, Haifa 3200003, Israel

David Keisar

Department of Mechanical Engineering, Massachusetts Institute of Technology Cambridge, Massachusetts, USA

David Greenblatt

Faculty of Mechanical Engineering, Technion – Israel Institute of Technology

Technion City, Haifa 3200003, Israel

Corresponding author: davidg@technion.ac.il

Abstract

A two-element natural laminar flow (NLF) airfoil – commonly used on medium-altitude, long-endurance, unmanned air vehicles – was conformally decambered for application on a two-bladed, H-rotor, vertical axis wind turbine. Blade kinematics were used to determine the virtual camber-line, which was then used to conformally map the original profile onto the chord-line, thereby virtually representing the original profile. Both decambered and original blade profiles were evaluated experimentally using large chord-radius ratios (0.6 and 0.75) that exploit the phenomenon of dynamic stall to produce the driving torque. Decambered blades showed substantially greater power and torque coefficients than the original blades, up to 60% and 27% respectively, which represents the first experimental validation of conformal decambering. Relatively large peak power coefficients of 28% were attained, despite maximum chord-based Reynolds numbers being less than 2.0×10^5. Depending upon the chord-radius ratio, light or deep dynamic stall occurs in the second upstream quadrant, and the flap flow remains attached virtually throughout. In contrast, on the original profiles, massive separation was observed on the blades, and the flap flow remained separated due to outer surface flow separation. Future research should consider surface pressure and flowfield measurements, significantly higher Reynolds numbers, and variable intra-cycle flap deflection mechanisms should be implemented to optimize performance and minimize unsteady loads.

1 Introduction

Vertical axis wind turbines (VAWTs) attract a great deal of attention from researchers, but have not as yet proven viable for large-scale wind energy production [1]. One area where VAWTs can compete is in the field of small-scale (typically less than 100 kW) grid-connected and off-grid applications [2-4]. In particular, lift-based high solidity machines ($\sigma \equiv Nc/R > 0.4$, where N is the number of blades, c is the blade chord-length and R is the turbine radius) have the advantage of low rotational speeds ω [5], which render them relatively quiet and bird-friendly [6]. They are, however, aerodynamically inefficient when compared to their horizontal axis (HAWT) counterparts [2]. Owing to the low blade-speed to wind-speed ratios (also called tip-speed ratios) $\lambda \equiv \omega R / U_\infty$ associated with high σ turbines, a central difficulty relates to maintaining efficient lift generation over a large angle-of-attack range $(\Delta\alpha)$. Not surprisingly, many different attempts have been made to increase VAWT performance, including blade profile shape optimization [8,9], passive flow control [10-12], variable pitch [13,14], active flow control [15-17] and turbine solidity variation [5,18].

Solidity can be varied by either increasing N or the chord-radius ratio $\varepsilon \equiv c/R$, and this is an important distinction, because when the chord-radius ratio exceeds some value, in the vicinity of $\varepsilon \approx 0.5$, the major fraction of the torque that spins the turbine derives from the phenomenon of dynamic stall. This should be contrasted with high-solidity turbines with $\varepsilon < 0.5$, where light stall is beneficial, but vortex shedding is considered to have a detrimental effect on efficiency [19]. This seemingly contradictory finding was observed in [20] and explained by [24] as follows: during rapid pitch-up, an aft dynamic stall vortex (ADSV) and a leading-edge (dynamic stall) vortex (LEV) form that produce high lift and low drag when the relative dynamic pressure is high; followed by shedding of the vortices when the dynamic pressure is low.

Another major factor affecting turbines with large ε, is curvilinear flow effects, first identified by Migliore et al. [25], where the relative velocity vector (angle-of-attack and magnitude) varies along the chord length. They proposed the use of conformal mapping techniques to transform the curvilinear problem into a rectilinear one, thereby introducing the concepts of "virtual angle-of-attack" $\alpha' = \alpha'(x)$ and "virtual camber" $z' = z'(x)$. Thus, airfoils optimized in rectilinear flow can be conformally mapped into the *de facto* blade profile, and we refer to this as conformal decambering. These effects were examined computationally [26,27], where design criteria were proposed and the virtual effects were quantified for different airfoils, ε, and λ. Another important feature of high solidity turbines is that virtually the all of the useful torque is produced in the upwind quadrants, while the blades in the downwind quadrants produce little, or even negative, torque [28-30]. Thus, only positive angles of attack need to be considered when selecting a conventional, rectilinear flow, airfoil profile.

The objective of this research is to design and experimentally evaluate an efficient high-ε VAWT that is driven by dynamic stall. Excellent candidates for such turbines are two-element (slotted) natural laminar flow (NLF) airfoils, because a large fraction of the chord-length on both surfaces is laminar and the slot reinitiates laminar flow on the flap. Symmetric NLF airfoils were developed for low solidity Darrieus turbines [31] and, more recently, several computational studies have investigated slotted and multi-airfoil arrangements [32-35]. Our research is fundamentally different from these studies in two respects: first, we employ asymmetric slotted NLF blade profiles, originally designed for medium-altitude long-endurance (MALE) unmanned air vehicles (UAVs) [38]; and second, we adapt these profiles to high-ε VAWTs using conformal decambering [25], which is a critical design step. Neither of these two factors have been experimentally studied previously.

This paper is structured as follows: section 2 briefly describes the basis of VAWTs driven by dynamic stall; section 3 introduces the slotted NLF airfoil and the conformal decambering technique; section 4 describes the test turbine, measurement techniques and wind tunnel setup; section 5 discusses the results based on performance metrics and flow visualization; and section 6 presents the main conclusions.

2 VAWT Driven by Dynamic Stall

It has long been known that dynamic stall increases localized peak aerodynamic torque on low solidity VAWTs, particularly in the upwind quadrants [36] and it can increase average turbine power by approximately 15% [37]. While stall is generally associated with performance losses in turbomachinery, the VAWT is a unique in that dynamic stall increases performance. This is because during pitch-up the static maximum lift is exceeded, often significantly, followed by dynamic separation of the flow. The downside of this process is that the larger peak load oscillations compromise the reliability of the drive-train and affect generator sizing [37]. However, on small-scale high solidity machines, where $\lambda \approx 1$, these loads may be manageable by judicious design of the drivetrain and suspension.

If we select turbines with large chord-to-radius ratios $\varepsilon \gtrsim 0.5$, then virtually all of the turbine torque is, in fact, developed as a result dynamic stall. To illustrate this, consider the phase-averaged, particle image velocimetry, flowfield measurements inboard of the upstream blade of a two-bladed H-rotor VAWT with $\varepsilon = 0.6$ at an azimuthal angle $\theta = 120°$, adapted from [20], shown in Fig. 1. The velocity vectors (u, v) in blade-fixed coordinates (x, y) were obtained by adding the blade velocity ωR to the measured velocity field so as to render the them in the coordinates of a stationary blade; and dimensionless vorticity was calculated according to $\zeta_z c / U_\infty \equiv (\partial v / \partial x - \partial u / \partial y) c / U_\infty$. The successive measurements (top to bottom) correspond to increased turbine loading, which leads to lower λ, higher power coefficients C_P, and more advanced shedding of the dynamic stall vortices. Here $C_P \equiv P / q_\infty U_\infty A$, where q_∞ is the freestream dynamic pressure, P is the turbine's power, and A is the turbine's projected area. By the conventional rules of turbomachinery, power should not increase with more advanced shedding of the vortices, because separation negatively impacts the aerodynamic coefficients, i.e., decrease the blade lift coefficients and increase the blade drag coefficients [21]. The reason this is not the case is because significant static-lift overshoot is produced in the first quadrant $(0° \le \theta \le 90°)$, when the dynamic pressure is relatively high; while vortex shedding occurs in the second quadrant $(90° \le \theta \le 180°)$, when the dynamic pressure is relatively low. Thus, the deleterious effects on the *aerodynamic coefficients* play only a minor role due to low relative dynamic pressure, particularly as $\lambda \to 1$ [21,23]. Further increases in turbine loading (not shown) causes a decrease in torque because the positive torque-producing effects of dynamic stall are negated by the adverse torque-retarding effects. A final aspect to note in Fig. 1 is the highly deflected shear layer at the trailing-edge, which has an adverse effect on turbine performance. An attempt to ameliorate this phenomenon is addressed in this paper.

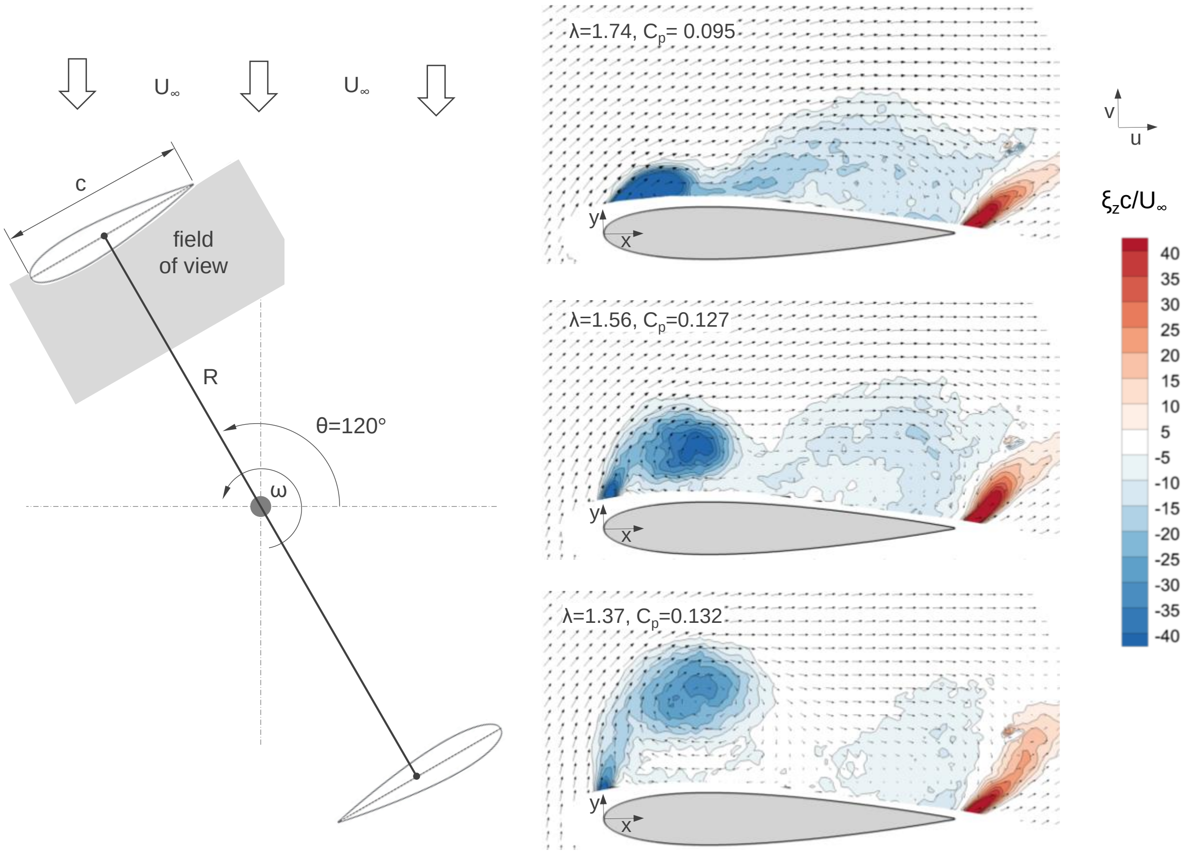

Fig. 1 Schematic of a two-bladed VAWT with $\varepsilon = 0.6$ showing the measurement field of view (left); and particle image velocimetry measurements of velocity vectors and derived dimensionless vorticity, inboard of the upstream turbine blade, for successive increases in loading (right). Adapted from [20].

3 Conformal Decambering of the NLF Profile

Two-element NLF airfoils are commonly used as the wing profiles of subsonic MALE UAVs, and many of their characteristics render them directly applicable to VAWTs [38]. In particular, high aspect ratio UAVs with appreciable parasitic drag attain maximum endurance at high lift coefficients C_l. This means that the airfoils must have high $C_{l,\max}$ and because they fly close to $C_{l,\max}$ they must have gentle stalling characteristics, for safety. Furthermore, they must have a high tolerance to surface fouling and a large internal volume, i.e., a thick section, for fuel storage. All of these factors are beneficial for high-ε VAWTs that are driven by dynamic stall: specifically, high $C_{l,\max}$ produces large torque; gentle stall ensures large post-stall torque generation and damps unsteady loading; performance degradation is minimal following inevitable fouling; and thick blades are structurally beneficial.

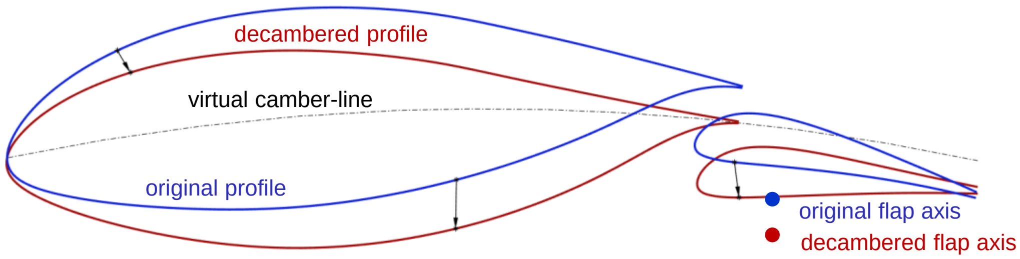

Fig. 2 Schematic of the original SA-21 profile, the virtual camber-line according to eqn. (1) and the conformally decambered airfoil (SA-21-D) with $\varepsilon = 0.6$, $x_c / c = 0.5$ and $\lambda / (1 - a) = 1.5$ [24]). Arrows indicate the transformation of arbitrary points for illustration.

For this research, we employ a modified version of the SA-21 shown in Fig. 2 (the blue line corresponds to the original profile), which has a thickness of 21%, and is comprised of a main element and slotted flap [38]. The airfoil is designed for $Re = 10^6$, with a $C_{l,\max} = 2.4$ and a large positive-lift angle-of-attack range of 21°. The large leading-edge radius, combined with flap slot, ensures gentle stall characteristics. When the surface is aerodynamically smooth, laminar flow extends over 60% and 80% of the upper (low pressure) and lower (high pressure) airfoil surfaces, respectively, producing a high aerodynamic efficiency/lift coefficient combination ($C_l / C_d \approx 150$ at $C_l \approx 2$). The effects of roughness due to wear and fouling are ameliorated somewhat due to the flow through the gap, which a produces a high momentum-flux jet over the flap, which is also expected to counteract the highly deflected turbine-blade trailing-edge shear layer, shown in Fig. 1.

In order to modify the profile to account for virtual camber with large ε, consider the blade kinematics shown for the upwind, torque-producing, half of the azimuth shown in Fig. 3 (see [24]). In the figure, V_b is the blade speed at the strut-blade connection point x_c, U_i is the average induced velocity (assumed constant across the diameter) and W is the velocity relative to the blade at x_c. From the kinematics, the virtual angle of attack is denoted α' and hence the virtual camber-line slope is:

$$dz'/dx = \tan^{-1}\left(\frac{\sin(\theta+\beta')}{\lambda/(1-\bar{a})+\cos(\theta+\beta')}\right) - \tan^{-1}\left(\frac{\sin\theta}{\lambda/(1-\bar{a})+\cos\theta}\right) - \beta' \qquad (1)$$

where $\bar{a} \equiv 1-\bar{U}_i/U_\infty$ is the average induction factor and

$$\beta' = \tan^{-1}\left(\frac{x_c - x}{c}\frac{c}{R}\right) \qquad (2)$$

The corresponding relative dynamic pressure along the chord-length is:

$$q_{\text{rel}} \equiv \tfrac{1}{2}\rho|W|^2 = \tfrac{1}{2}\rho U_\infty^2\{[\lambda/(1-\bar{a})+\cos(\theta+\beta')]^2+\sin^2(\theta+\beta')\} \qquad (3)$$

The conformal transformation of a symmetric profile introduced by [25] and applied computationally by [26,27], was achieved by fitting its chord-line to that of a circular arc, based on average azimuthal values. Our approach is different and based on a design-point transformation, according to eqn. (1) and for this we must select a geometric configuration, namely ε_d and $(x_c/c)_d$, as well as a design-speed parameter $\lambda'_d \equiv \lambda_d/(1-\bar{a}_d)$ close to $C_{P,\max}$. The first two parameters are geometric and therefore readily defined based on our preliminary data [3,24,39], namely $\varepsilon_d = 0.6$, $(x_c/c)_d = 0.5$. For the purpose of our design, we select $\lambda_d = 1$ and $\bar{a}_d = \tfrac{1}{3}$ (corresponding to the Betz limit), to give $\lambda'_d = 1.5$. Using these parameters, numerical integration of eqn. (1) is performed using a 4$^{\text{th}}$ order Runge-Kutta method for $\theta = 0°$, $90°$ and $120°$ and the results are shown in Fig. 4. It can be seen that the virtual camber-line is weakly dependent on θ, and we choose the result at $\theta = 90°$ as being sufficiently representative, or average, for our design. Conformal decambering (red line in Fig. 2) was accomplished by mapping the original profile based on decambering the $\theta = 90°$ virtual camber-line to the chord-line ($z/c = 0$), while preserving the angles between the airfoil geometry and the lines normal to the camber-line. We designate the decambered airfoil: SA-21-D. The camber-line function can be adequately represented by a parabolic function with a maximum camber of approximately 5%, and this will be shown formally in section 5.4.

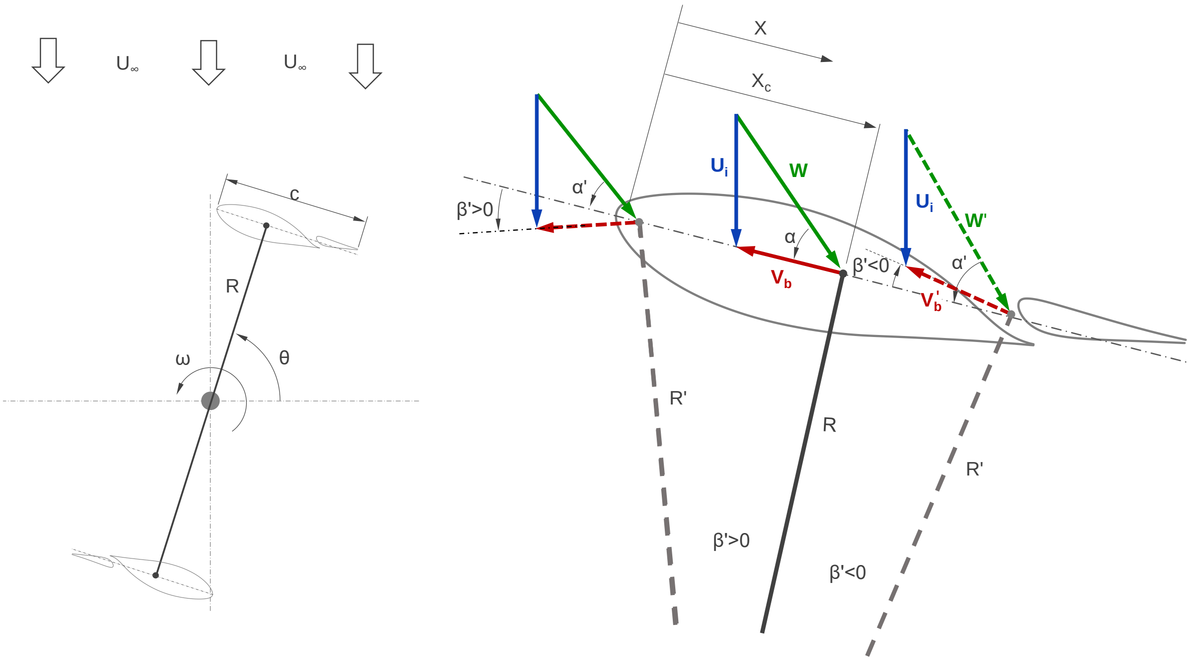

Fig. 3 Schematic VAWT illustration adapted from [24] of the conformably decambered SA-21 blade profile geometry with relevant geometric and angular definitions (left) and velocity triangles corresponding the upwind blade (right).

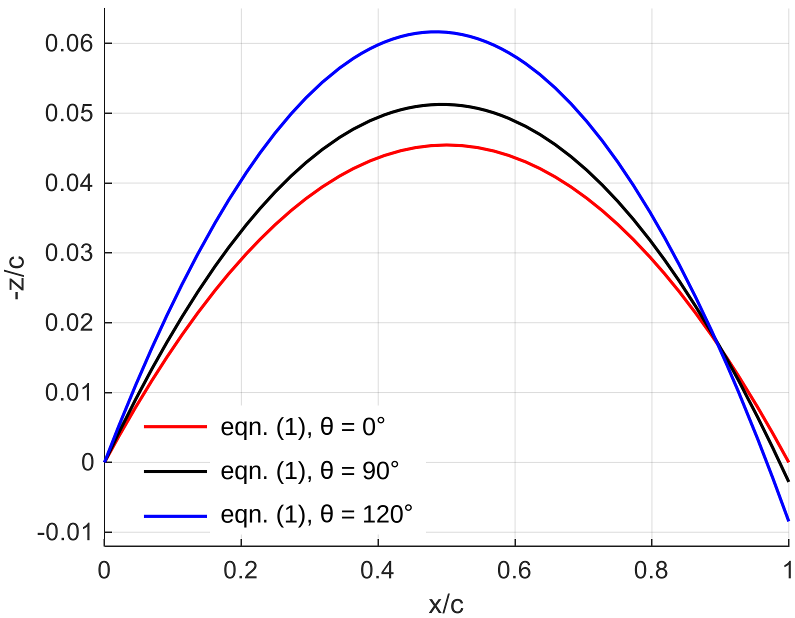

Fig. 4 Virtual camber-lines based in the integration of eqn. (1) for several azimuthal angles with $\lambda_d' = 1.5$**.**

4 Experimental Setup

Experiments were conducted in the test section of a blow-down wind tunnel, where the original 1.0 m × 0.61 m configuration [40] was replaced by a 1.0 m × 1.9 m test section. This resulted in a maximum wind speed of $U_\infty = 16$ m/s, a relative standard deviation distortion of 1.4% and a turbulence level of 0.5%. The test turbine, shown schematically in Fig. 5, was designed to accommodate multiple, blade and geometric configurations. It was comprised of aluminum shaft (diameter $d = 50.6$ mm), located in the center of the test section, to which the blades were connected by means of adjustable-length stainless-steel struts. The shaft was secured above and below the test section on two self-aligning ball bearings. To avoid excessive deformation of the shaft, wind tunnel speeds were limited to $U_\infty \leq 6$ m/s.

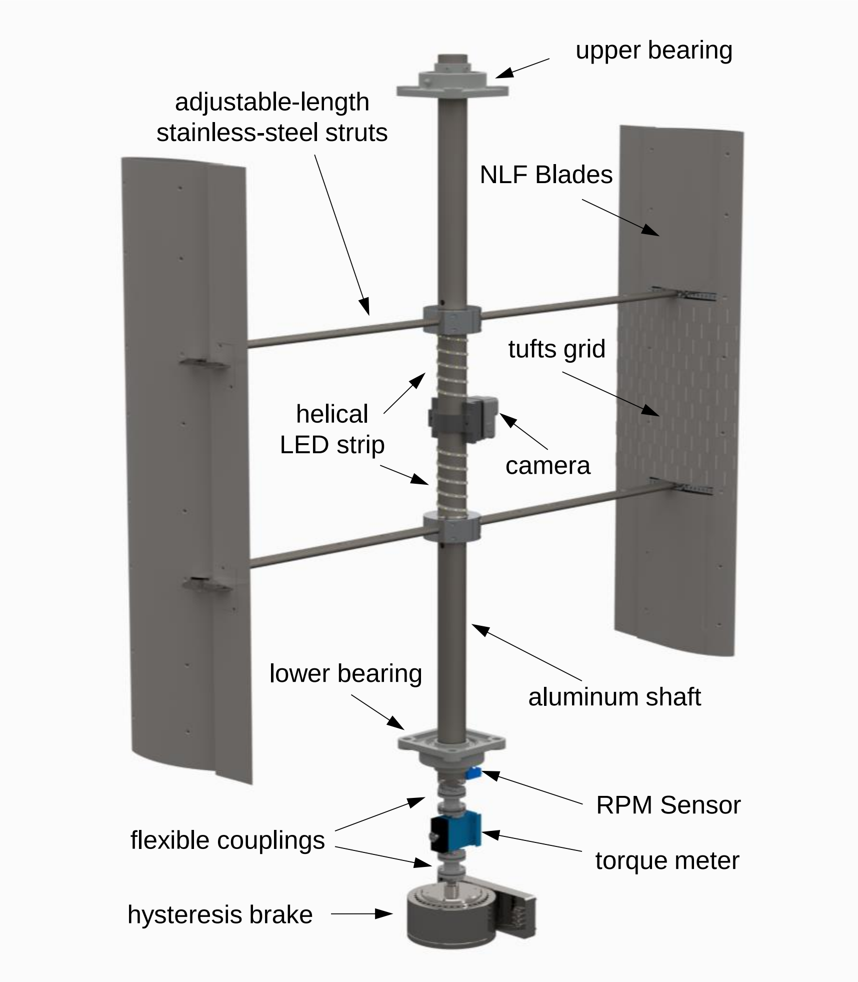

Fig. 5 Schematic of the test turbine showing the main components and measurement instrumentation. Tufts and camera were only implemented for flow visualization experiments.

Turbine performance was measured using two blade-types: the original SA-21 profile and the conformally decambered SA-21-D described in the previous section. Both blade-types had identical dimensions, namely chord length $c = 300$ mm span $b = 970$ mm , and both were evaluated with strut-lengths of $R = 400$ and 500 mm ($\varepsilon = 0.75$ and 0.6, respectively), with the projected area defined as $A = 2Rb.$ The main-element of each blade was constructed using two aluminum ribs that were bolted to two load-bearing cylindrical (20 mm diameter) carbon fiber spars as shown in Fig. 6. The inboard sides of the ribs were equipped with 16, 5 mm holes with insert threads. These were connected to the struts using small flanges, and allowed variation of the strut-blade connection point in the range $0.13 \le x_c / c \le 0.63.$ Six additional ribs, used to maintain the integrity of the blade geometry, were 3D printed from Polylactic Acid (PLA) and screwed into the spars. The outer shell of each blade comprised four, 2 mm thick, 3D printed PLA segments that locked together by mating slots and glued. The shell assembly was then screwed to the eight (two aluminum and Six PLA) ribs.

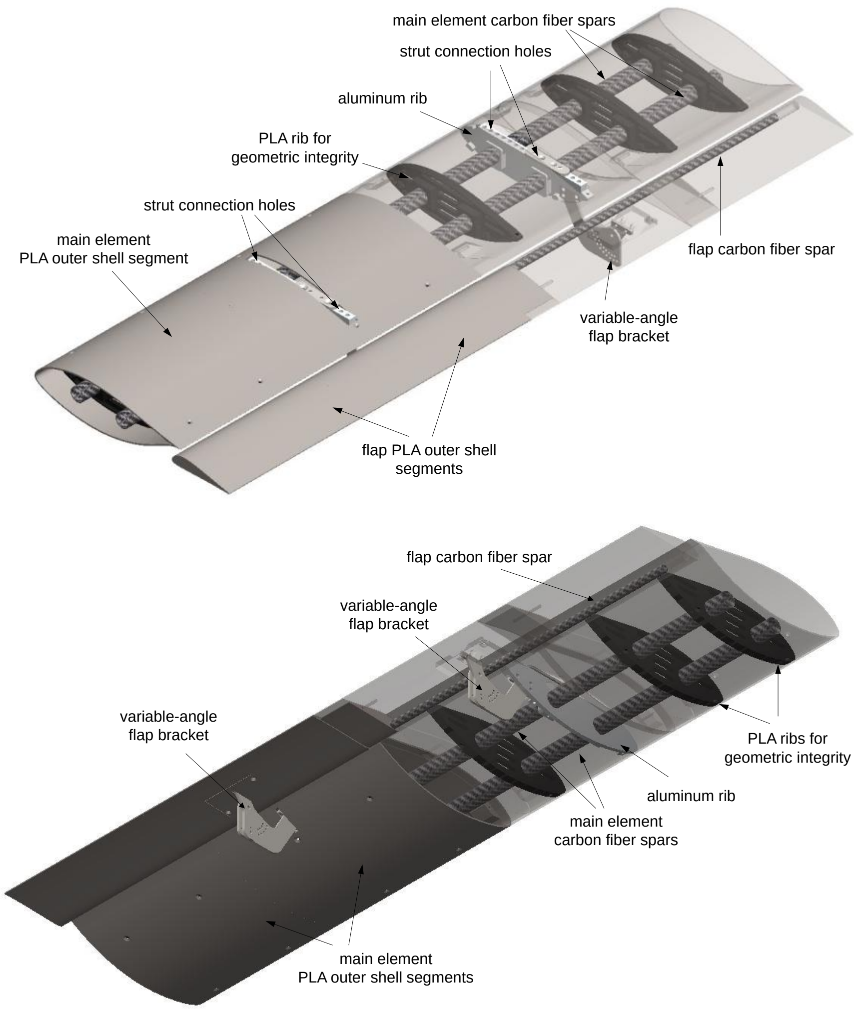

Fig. 6 Details of the SA-21-D blade construction and materials with upper halves partially transparent – top: inner surface of the blade; bottom: outer surface of the blade.

The flaps shells were also 3D printed from PLA segments with mating slots, that were glued together, and the assembly was bolted to a 10 mm diameter carbon fiber rod (see Fig. 6). Flap brackets, used for securing the flap to the main element and adjusting the flap angle, were manufactured from 3 mm thick stainless-steel plates and comprised two main parts. One part was bolted to the aluminum ribs on the main element, and one part was bolted to printed brackets on the flap. They were joined together at the flap axis by a short, threaded rod. Two rows of holes were drilled on each of the parts, which facilitated fixed flap angle settings between –20° and +70°, in steps of 5°. All blades were set at a nominal pitch angle $\beta = 0°$ and connected at the profile mid-chord $x_c / c = 0.5$. In the experiments presented here, flap deflections of –5°, 0° and 5° were considered.

The turbine was loaded using a custom dynamometer, that comprised a HB-140M2 Magtrol 10 Nm hysteresis magnetic brake and a Kistler 4502A10RAU (10±0.02 Nm) torque (T) meter (see Fig. 5). Torque was transmitted to and from the torque meter via two sets of flexible couplings. Rotational speed (f) was measured using a KFPS TL proximity sensor, facilitating the calculation of power $P = T\omega$, where $\omega = 2\pi f$. The majority of experiments were performed at nominal wind velocity of $U_\infty = 2.7\,\text{m/s}$, with additional experiments in the range $2.7\,\text{m/s} \le U_\infty \le 5.4\,\text{m/s}$. All wind speeds were measured to within attained ±0.15 m/s and wind tunnel blockage corrections were performed according to the method of [41]. Results were evaluated on the basis of power and torque coefficients – defined as $C_P \equiv P / q_\infty U_\infty A$ and $C_T \equiv T / q_\infty AR$, – as a function of λ.

Selected flow visualization was performed using an array of 25mm-long fluorescent polyester tufts. They were attached horizontally, i.e., in the chordwise direction, and staggered on the blade main-element (10 rows) and flap (3 rows). The surface was painted matt-black and the tufts were attached using 75 µm polyamide tape. Uniform illumination of the tufts was achieved by using white-light LED strips that were wound around the shaft in a helical fashion. The LEDs were powered by a 3S LiPo battery, also mounted on the shaft. A GoPro™ Hero 9 camera was mounted on the shaft and oriented normal to a blade chord-line. Images were acquired at 240 frames per second and triggered at $\theta = 0°$ to allow subsequent binning and analysis. Turbine performance with and without tufts did not vary outside of the evaluated experimental uncertainty.

5 Results and Discussion

5.1 Turbine Performance

Power and torque coefficient characterization, both uncorrected and corrected for blockage effects, are shown for both blade profiles at the design point $\varepsilon_d = 0.6$ in Fig. 7. Large effects of correction are evident for both coefficients as well as for the speed-ratio λ due to the relatively large blockage ratios. Overall, the corrected coefficients corresponding to decambered SA-21-D blades produce substantially greater peak power and torque than those of the original SA-21 blades, namely $\Delta C_P \approx 60\%$ and $\Delta C_T \approx 27\%$. These peak values are attained at higher λ maximum values and the λ range is greater. These substantial improvements conclusively validate the conformal decambering method, implemented to account for virtual camber, described in section 3. It is also notable that the peak C_P values are relatively high, even though the corresponding uncorrected Reynolds numbers are relatively low. On large turbines, where the minimum chord-based Reynolds numbers $Re_c \equiv |W|c/\nu$ are high, typically >10^6, Reynolds number effects are minor. However, on small high-ε turbines, there is an enormous variation from $U_\infty(1+\lambda')c/\nu$ at $\theta = 0°$ to $U_\infty(1-\lambda')c/\nu$ at $\theta = 180°$ as seen in eqn. (3). Furthermore, the local Reynolds number varies along the chord. An average Reynolds number can be defined for convenience, namely $\overline{Re}_c \equiv |\bar{W}|c/\nu \approx \lambda U_\infty c/\nu = \omega Rc/\nu$, but this average does not provide any insight into the aerodynamics [42]. We therefore define a maximum Reynolds number $Re_{c,\max} \equiv U_\infty(1+\lambda)c/\nu$ as being representative, because the important torque-producing aerodynamic effects occur in the first quadrant.

A negative (upward) flap deflection –5° has a small effect on peak torque and power for both profiles, and the main effect is an increase in the maximum values of λ. This is because negative flap deflections tend to reduce base-drag and is explained as follows. The original SA-21 airfoil was designed to obtain high endurance factors $C_l^{1.5}/C_d$ at corresponding high lift coefficients high C_l [38]. This is because aircraft with a combination of large aspect ratios and large base-drag coefficients require this combination to maximize flight time [43]. However, negative flap deflections are set for high-speed subsonic flight at low angles-of-attack, where high aerodynamic efficiency C_l/C_d is required at low C_l [38,43]. This simultaneously reduces base drag C_{d0} and $C_{l,\max}$ on the airfoil; on the wind turbine this translates to higher rotational speeds without a significant change in peak power.

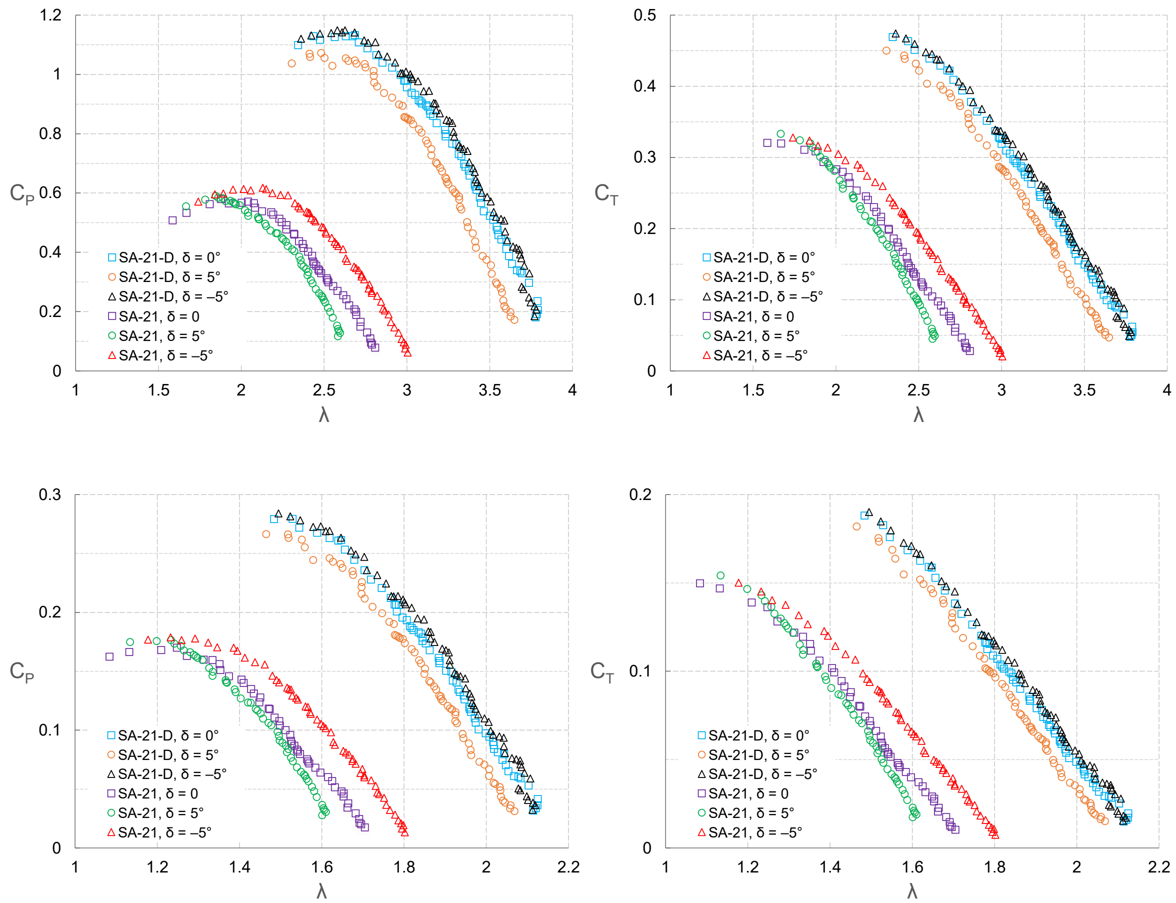

Fig. 7 Power and torque coefficients as a function of speed-ratio for $\varepsilon = 0.6$ and $U_\infty = 2.75$ m/s – top row: uncorrected data; bottom row: corrected for wind tunnel blockage according to [41].

The corresponding turbine performance results at $\varepsilon = 0.75$ (Fig. 8) are qualitatively similar to those at $\varepsilon = 0.6$ (Fig. 7), but with notable quantitative differences. In particular, the torque coefficients are higher, as expected, and both original and decambered cases attain peak C_T and C_P at similar λ. The uncorrected C_T results also exhibit a change in slope at $\lambda \approx 2.2$ and this may be due to excessive virtual camber that precipitates early dynamic stall. This can be understood by noting that the maximum virtual camber $z'_{\max} \propto \varepsilon$ (see eqn. (1) and section 5.4) and hence decambering described in section 3 should be 25% greater for $\varepsilon = 0.75$. Nevertheless, the fact that the values are comparable at both values of ε, indicates that increased decamber would not produce significantly different results. Also note that the differences between the cambered and decambered peak performance results are smaller, namely $\Delta C_P \approx 30\%$ and $\Delta C_T \approx 20\%$.

For the uncorrected data resented in Fig. 7 and Fig. 8, we can assume that $\bar{a} < ⅓$ because the relatively large wind tunnel blockage ratio restricts divergence of the streamlines around the turbine. However, the blockage-corrected coefficients and speed-ratio shown in Fig. 7 and Fig. 8 do not reflect the *de facto* aerodynamics under those conditions, but rather the under the corresponding uncorrected conditions. This impacts the dynamic-stall-based torque generation mechanism by reducing the peak angle-of-attack, dynamic pitchrate and dynamic pressure excursions, while increasing the Reynolds number. Thus, the blade aerodynamics is driven by conditions at $\lambda \approx 2.5$ (Fig. 7) instead of those at $\lambda = 1.5$; hence the peak angle-of-attack drops from $\alpha \approx 42°$ to $\alpha \approx 24°$ and the relative dynamic pressure q_{rel} drops to approximately 8% of its peak value, and not 4%. Future experiments performed using these blades should seek to eliminate or drastically reduce wind tunnel blockage effects.

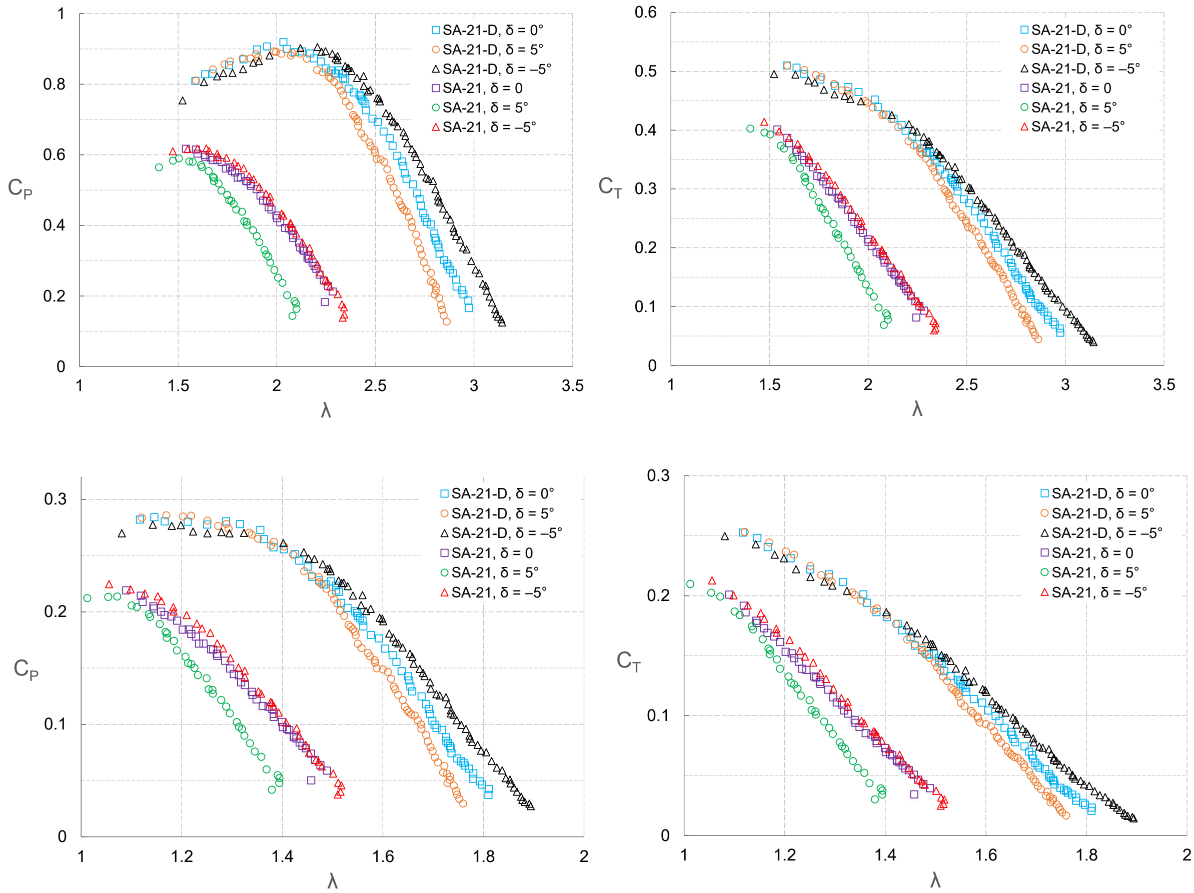

Fig. 8 Power and torque coefficients as a function of speed-ratio for $\varepsilon = 0.75$ and $U_\infty = 2.75$ m/s – top row: uncorrected data; bottom row: corrected for wind tunnel blockage according to [41].

The results presented above are conservative and likely representative of a wind turbine in a high turbulence environment where the blade surface finish is not aerodynamically smooth. This can be understood with respect to aerodynamic parameters based on wind tunnel experiments performed on the SA-21 and shown in Table 1 [38]. In these experiments, the turbulence level was ~0.1% and the effect of #150 grit roughness at 5% chord, on the upper (low pressure) surface, was investigated. With roughness, the primary aerodynamic parameters, namely peak efficiency $(L/D)_{\max}$, C_l at $(L/D)_{\max}$, $C_{l,\max}$ and α_{stall} , remain reasonably high, but are substantially lower than the aerodynamically smooth conditions. In our experiments, the turbulence level is 0.5%, and the surface finish is between Ra 1.1 and 1.6 (i.e., average surface roughness in microns), which is an order of magnitude greater than [38]; hence, this will undoubtedly affect performance negatively. It can therefore be expected that experiments performed at low turbulence levels, on an aerodynamically smooth SA-21-D, will produce significantly improved performance.

Table 1. Aerodynamic parameters for the SA-21 airfoil at $Re_c = 10^6$ and turbulence level of ~0.1%, corresponding to an aerodynamically smooth surface and a roughness strip at 5% chord on the upper (low pressure) surface [38].

	$(L/D)_{\max}$	C_l @ $(L/D)_{\max}$	$C_{l,\max}$	α_{stall}
aerodynamically smooth	150	2.0	2.4	13°
#150 standard roughness grit	80	1.6	1.9	10°

Keisar et al. [39] conducted a detailed parametric study of NACA 0012 and NACA 0021 blade profiles under the conditions considered here, with the addition of the geometric blade preset angle β, blade offset x_c/c, extended chord-radius ratio ε and Reynolds number. At low Reynolds numbers, NACA 0021 profile performance was vastly superior to that of the NACA 0012 profile, due to profound differences in stalling characteristics [44], namely trailing-edge versus leading-edge stall. The maximum values of C_P for the NACA 0021 were attained under the conditions $\varepsilon = 0.75$ and $2° \le \beta \le 4°$, and these data are compared to the corresponding SA-21-D data in Fig. 9 for the range of Reynolds numbers considered in this study (see section 4). At relatively low Reynolds numbers, approximately $Re_{c,\max} < 2\times10^5$, the NACA 0021 blades attain higher values of C_P and C_T, but the SA-21-D has a greater positive sensitivity to Reynolds number. The poorer SA-21-D performance at low Reynolds numbers is most likely due to premature separation, because the design Reynolds number for this profile is 10^6 [38]. The result is that the design point streamwise extents of laminar flow are not maintained on either or both of the main element surfaces, and hence the laminar separation bubbles burst. Nevertheless, the performance does not drop dramatically because the flap slot, at least partially, re-energizes the laminar flap boundary layer (see section 5.2). We can expect that further increases in Reynolds number, not possible in the present experimental setup, will produce substantial increases in performance. This expectation is based on the data in [38], where $C_{l,\max}$ increases from 2.27 to 2.40 and the endurance factor increases by 60% with an increase from $Re_c = 4\times10^5$ to 1.4×10^6. Furthermore, high solidity experiments performed by Miller et al. [5], employing NACA 0021 profiles, revealed that the peak power coefficient increases by approximately 67% as the Reynolds number increases by an order of magnitude from 2×10^5.

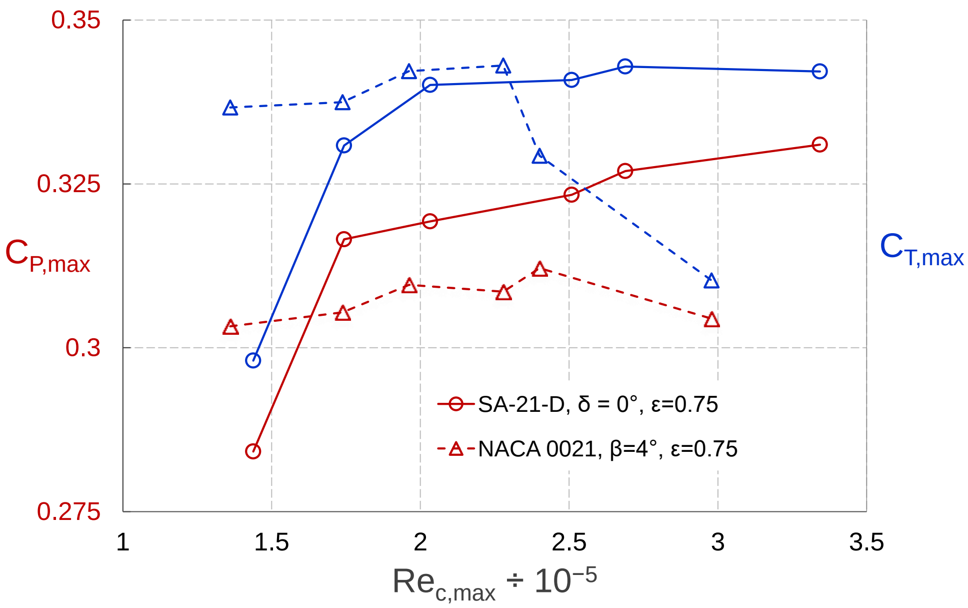

Fig. 9. Corrected peak power coefficients as a function of Reynolds number $Re_{c,\max} \equiv U_\infty c(1+\lambda)/\nu$ **corresponding to the freestream velocity range** $2.75 \text{ m/s} \le U_\infty \le 6 \text{ m/s}$. **NACA 0021 data from [39].**

5.2 Flow Visualization

Tuft-based flow visualization on the inner surface of the original (SA-21) and decambered (SA-21-D) blades are shown for the upstream quadrants at $\varepsilon = 0.6$ in Fig. 10 for the azimuthal angles: $0° \le \theta \le 90°$ (top row), $90° \le \theta \le 120°$ (middle row) and $120° \le \theta \le 180°$ (bottom row). The video images were binned at successive azimuthal angles θ with an uncertainty of $\pm 1°$ and then color-coded from red to blue for the indicated azimuthal range. The main-element trailing-edge location is indicated by the vertical dashed grey lines, to distinguish between the main-element and flap tufts. The tuft images in Fig. 10 correspond to the peak power coefficients shown in Fig. 7.

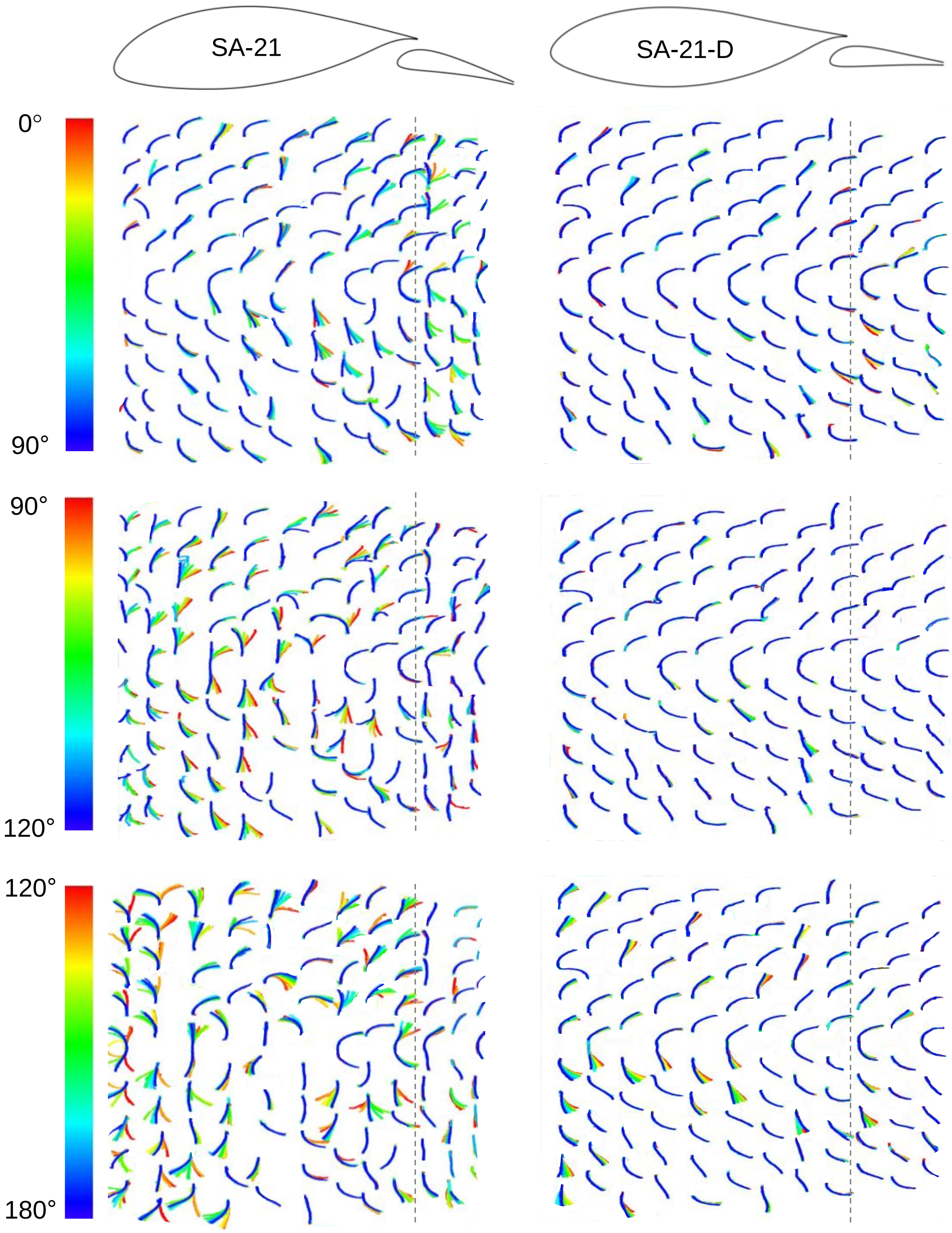

Fig. 10. Color-coded tuft-based flow visualization based on angular binning in the upstream quadrants for the SA-21 and SA-21-D blade profiles ($\varepsilon = 0.6$ and $U_\infty = 2.75$ m/s). Vertical grey dashed line corresponds to the main-element trailing-edges.

On the decambered blades, the tufts indicate that the flow is virtually fully attached in the first quadrant, i.e., with a few exceptions, the flap tufts are deflected downstream and no movement of the tufts is detected. The movement of some tufts near the main-element trailing-edge and on the flap is due to reattachment, which follows local separation when the blade traverses the downwind quadrants (not shown). In contrast, on the original profile, there is strong evidence of separation on the aft part of the main element and on the flap in the first quadrant, as the tuft point upstream with increasing azimuthal angle. The most probable reason for both of these observations is the additional virtual camber imposed on the already highly cambered original SA-21 airfoil. On the main element inner (low-pressure) surface, this is due directly to high surface curvature; while on the flap, outer (high-pressure) surface leading-edge separation due to excessive camber (geometric + virtual) weakens the passive slot blowing effect. This is because the effectiveness of the passive flap blowing slot, relies on an attached boundary layer to be effective. Highly cambered airfoils are known to suffer from lower surface separation at low angles-of-attack [45,46]. In the azimuthal range $90° \le \theta \le 120°$, the decambered flow remains almost completely attached, with only a small local movement of the tufts on the aft part of the main element. This is indicative of mild aft main-element stall. In contrast, the original profile shows massive separation during the entire second quadrant $(90° \le \theta \le 180°)$ over the entire extent of the main element, while the flap flow also remains fully separated. Tufts on the decambered profile for $120° \le \theta \le 180°$, however, show mild main-element separation and the beginning of leading-edge stall at $\theta \approx 180°$. We can conclude, therefore, that dynamic stall is very mild, mainly on the main element downstream of the leading-edge, and the leading-edge DSV forms as $\theta \to 180°$.

The fact that the vortex is not shed during the latter part of the second quadrant appears to contradict the tuft observation made by Keisar et al. [24], who observed vortex shedding in the second quadrant. As discussed above in section 5.1, the most likely reason for this is the effect of wind tunnel blockage, where the peak uncorrected power coefficient data and flow visualization are acquired at $\lambda \approx 2.5$, not $\lambda = 1.5$. In the case of [24], the wind tunnel blockage was 0.16 – versus 0.49 in these experiments – and hence blockage corrections were negligible.

Additional flow visualization, shown in Fig. 11, was performed at $\varepsilon = 0.75$ and uncorrected $\lambda = 1.6$, which is closer to our original design speed. These images correspond to the peak power coefficients shown in Fig. 8 and the azimuthal angle binning shown is identical to that shown in Fig. 10. In the first quadrant, the main difference, when compared to the

$\varepsilon = 0.6$ visualization, is that the flap flow is attached or reattaches on the decambered flap profile, while on the original profile it is separated as indicated by the oscillating tufts. Note, in addition, that at the beginning of the first quadrant, at $\theta \approx 0°$, the leading-edge tufts on the original profile are reattaching from the previously separated flow in the downstream quadrants (not shown). In the first segment of the second quadrant ($90° \le \theta \le 120°$), the difference between the two profiles in the leading-edge region is important. The decambered profile shows a larger degree of leading-edge separation, and this is consistent with the formation of a leading-edge vortex and consistent with the observations of [24]. In the vicinity of the mid-chord, slower movement of the tufts is also consistent with formation of the DSV. As in the first quadrant, the flap flow remains effectively attached, in contrast to the original profile, where the flap flow remains separated. During the final segment of the second quadrant $(90° \le \theta \le 120°)$ the decambered profile indicates full leading-edge stall, most likely associated with shedding of the DSV, while the flap remains mainly attached. In contrast, the original profile shows leading-edge stall, indicative of a DSV, even though the aft part of the main element and flap flows are separated, and this persists throughout the downstream quadrants (not shown).

Two additional points can be made about the flow visualization and its relationship to the data presented in Fig. 7 and Fig. 8. First, even though the original non-decambered profile exhibits massive separation throughout virtually the entire azimuth, it still produces useful torque, with power and torque coefficients that are comparable to other high-solidity VAWTs. Second, despite the significantly different flow states on the decambered profiles during relatively light stall at $\varepsilon = 0.6$ (Fig. 7 and Fig. 10) and relatively deep stall (Fig. 8 and Fig. 11), the $C_{P,\max}$ values are comparable, but $C_{T,\max}$ is higher in the latter case. High torque coefficients are particularly advantageous for self-starting or driving high-pressure pumps that are used for irrigation or desalination [3-4]. Therefore, from a purely performance-based point-of-view, deep dynamic stall has an advantage over light dynamic stall [19].

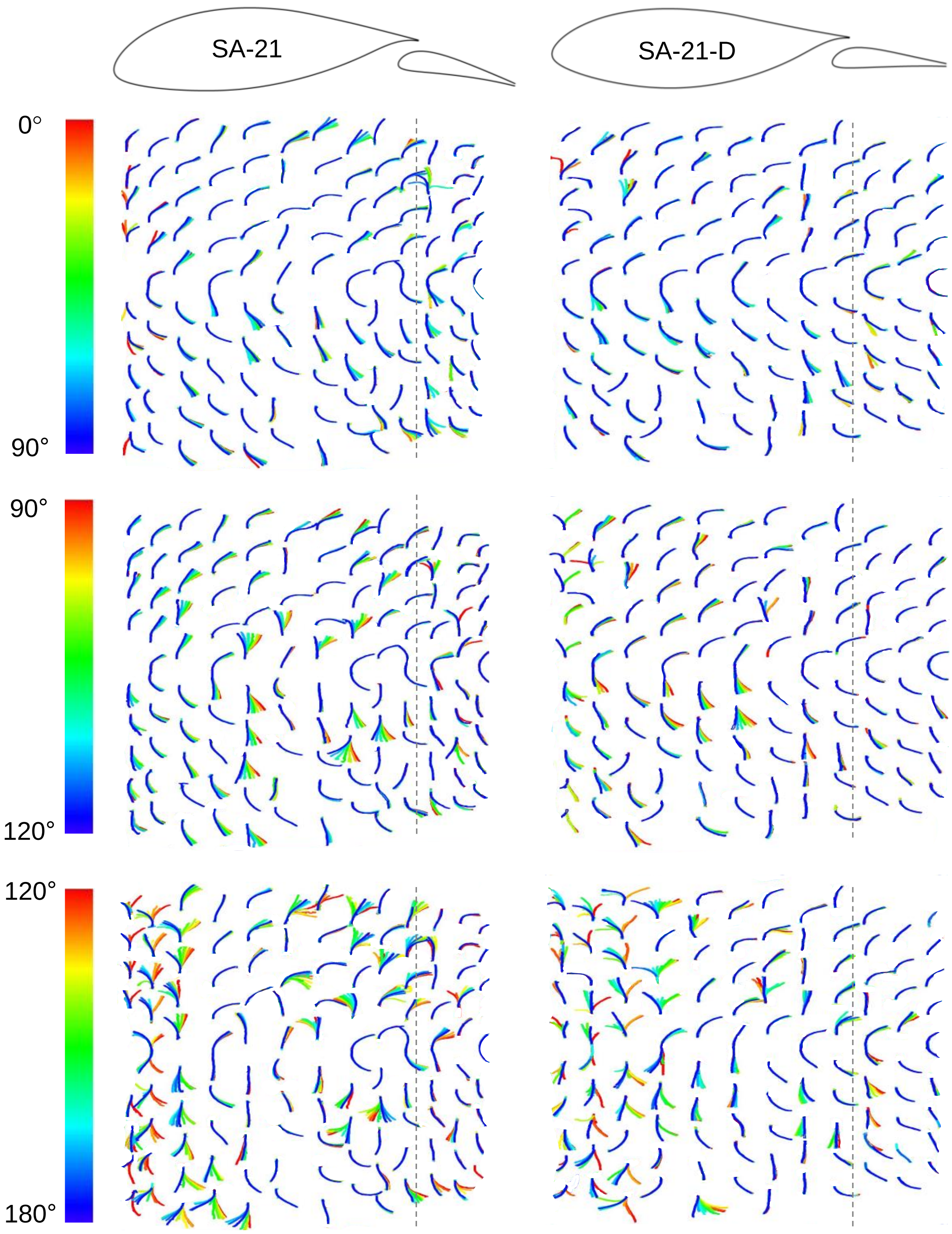

Fig. 11. Color-coded tuft-based flow visualization based on angular binning in the upstream quadrants for the SA-21 and SA-21-D blade profiles ($\varepsilon = 0.75$ and $U_\infty = 2.75$ m/s) . Vertical grey dashed line corresponds to the main-element trailing-edges.

5.3 Advantages & Modifications

Our use of the slotted NLF profile with large ε, and therefore, high solidity, was predicated on two factors: only positive lift angles-of-attack are important because useful torque is only generated in the upwind quadrants [28-30]; and (ii) high post-stall angles-of-attack result in gentle dynamic stall partly due to the partially attached flap. Moreover, the flap flow also counteracts the highly deflected streamlines that form at the at the trailing-edges of blades with high-ε as shown in Fig. 1 [20]. Note that this effect is amplified due to the increasing relative dynamic pressure along the chord. To simply illustrate this, let $\lambda' = 1$ in eqn. (3), resulting in:

$$q^* = \rho U_\infty^2 [1 + \cos(\theta + \beta')] \tag{4}$$

In the quadrants defined by $0° < \theta + \beta' < 180°$, the aft part of the blade beyond the mid-chord, namely $(x_c - x)/c = 0.5 - x/c < 0$, corresponds to $\beta' < 0$. Eqn. (4) shows, by inspection, that the relative dynamic pressure always increases for $\beta' < 0$. The result is a proportionately larger momentum flux through the slot, that increases the bound vortex strength and hence the torque. This effect is significantly smaller on turbines with low ε, and obviously absent on conventional flight vehicles where the freestream dynamic pressure is nominally constant. The variation in relative velocity along the turbine blade chord also indicates that the aerodynamics of a blade in curvilinear coordinates cannot, strictly speaking, be represented by the aerodynamics of a cambered blade in rectilinear coordinates, because the conformal transformation violates conservation of mass.

The slotted NFL profiles offer several advantages over single-element NLF profiles because the maximum lift coefficients of the latter are lower ($C_{L,\max} < 2$), and they have a limited positive-lift angle-of-attack range [47]. High-lift single-element airfoils $(C_{L,\max} > 2)$, on the other hand, are either highly cambered [45] or employ a laminar "rooftop" followed by a Stratford ramp [46]. Both varieties suffer from pressure surface stall at moderate angles-of-attack, which significantly increases drag, thereby limiting the effective angle-of-attack range $(\Delta\alpha < 15°)$. Moreover, single-element high-lift profiles suffer from severe performance losses due to surface roughness, which inevitably occurs due to wear and fouling.

Experiments performed with large flap angles, i.e., $\delta > 10°$, produced dramatic reductions in turbine speed and torque (not shown). Hence, large flap deflections can certainly be used to brake the turbine, much like the airbrake described in [38]. In future studies, variable flap intra-cycle flap deflections should be considered to optimize performance and minimize unsteady loads. This can be achieved by equipping the turbine blades with pressure sensors to resolve the blade torque as a function of the azimuthal angle. Then, closed-loop control can be implemented for optimization, for example using maximum power-point tracking [48]. Note furthermore that variable flap deflections are analogous to variable blade pitching that is known to improve self-starting and reduce unsteady loads on H-rotor VAWTs [13,14], but variable flap deflections present at least two advantages. First, they are much smaller and lighter than the main element, which allows simpler designs, smaller mechanism loads and faster response times. Second, the flap deflection mechanisms can be mounted within the main element, much like on an aircraft wing, and therefore not incur the added drag penalties of variable blade pitching mechanisms.

5.4 Simplified Camber-line Estimation

The ad-hoc parabolic profile referred to in section 3 can be generalized on the basis of theoretical and physical arguments. It was shown in Fig. 4 that the virtual camber line is weakly dependent upon the θ. In fact, when $\lambda/(1-\bar{a})=1$, it can be shown that $dz'/dx \neq f(\theta)$, if we ignore the singularities at $\theta+\beta'=180°$ and $\theta=180°$. To show this, eqn. (1) can be written as:

$$dz'/dx = \tan^{-1}\left(\tan\left(\frac{\theta+\beta'}{2}\right)\right) - \tan^{-1}\left(\tan\left(\frac{\theta}{2}\right)\right) - \beta' \tag{5}$$

We note furthermore, on physical grounds, that $q_{\text{rel}} \to 0$ at the singularities, and hence at these angles the blades do not produce useful torque. They are therefore of no practical interest and thus eqn. (5) can be written as:

$$dz'/dx = -\beta'/2 \tag{6}$$

which is independent of θ. Substituting eqn. (2) into eqn. (6) and integrating from $(x,z')=(0,0)$ produces the virtual camber-line:

$$\frac{z'}{c} = \frac{1}{4\varepsilon}\log\left(1+\frac{\varepsilon^2x^2-2\varepsilon xx_c}{\varepsilon^2x_c^2+c^2}\right) + \frac{x_c}{2c}\tan^{-1}\left(\frac{\varepsilon x_c}{c}\right) + \frac{x_c-x}{2c}\tan^{-1}\left(\frac{\varepsilon(x_c-x)}{c}\right) \tag{7}$$

The integration of eqn. (6) can be greatly simplified if we assume that $\beta'_{\max} << 1$, which results in the simple parabolic camber-line:

$$\frac{z'}{c} = \frac{x}{2c}\left(\frac{x}{2c}-\frac{x_c}{c}\right)\varepsilon \tag{8}$$

Finally, by solving eqn. (1) in the range of anticipated design points, namely $1 \le \lambda' \le 2.5$, and fitting least-squares curves to the $z'_{\max}$ values at $\theta = 90°$, a simplified and approximate relation can be used, namely:

$$\frac{z'}{c} \approx \frac{x}{2c}\left(\frac{x}{2c} - \frac{x_c}{c}\right)\left(0.75\ln\lambda' + 1\right)\varepsilon \tag{9}$$

6 Conclusions

An experimental investigation was conducted on a two-bladed, high-ε, H-rotor, VAWT employing slotted conformally decambered NLF blades, commonly used on MALE UAVs. Two sets of blades were evaluated: the original profile, known as the SA-21 airfoil; and a conformally decambered SA-21 airfoil, whose geometry was determined on the basis of design-point simplified blade kinematics. Large chord-radius ratios $\varepsilon = 0.6$ and 0.75, were selected so as to exploit the phenomenon of dynamic stall to drive the turbine and maximize performance. This research represented the first experimental validation of conformal decambering and the first adaptation slotted NFL blades to VAWTs.

A comparison of power and torque coefficients showed substantially greater peak values for the decambered profiles, namely $\Delta C_P = 60\%$ and 30%; and $\Delta C_P = 27\%$ and 20%, for $\varepsilon = 0.6$ and 0.75, respectively. And the decambered profiles attained relatively large power coefficients, $C_P = 0.28$, despite maximum blade Reynolds numbers less than 2.0×10^5. These observations effectively validated the decambering approach proposed here. Negative flap deflections had a small positive effect on peak torque and power for both profiles, and the main effect was an increase in the maximum rotational speed of the turbine due to reduced base-drag. Tuft-based flow visualizations for $\varepsilon = 0.6$ in the torque-producing upstream quadrants, showed very mild separation on the decambered profiles, with leading-edge dynamic stall vortex formation at $\theta \approx 180°$. This delay was attributed to wind tunnel blockage effects. In contrast, for $\varepsilon = 0.75$, the dynamic stall vortex forms in the $90° \le \theta \le 120°$ azimuthal range and sheds in the $120° \le \theta \le 180°$ range. In all cases, the flap flow was mainly attached. Large-scale separation was observed on the original profile at both $\varepsilon = 0.6$ and 0.75, and the flap remained entirely separated due to separation on the outer part of the blade. Despite this massive separation, a DSV was evident for $\varepsilon = 0.75$, with a peak power coefficient $C_P = 0.22$.

Future experiments should focus on phase-resolved surface pressure and flowfield measurements to obtain a better understanding of the aerodynamics. Performance evaluations should also be conducted with aerodynamically smooth blades, within a low turbulence environment, and at substantially higher Reynolds numbers, O(10^6), corresponding to the airfoil design point. In addition, variable, intra-cycle flap deflections should be considered to optimize performance and minimize unsteady loads.

References

1. Mollerstrom, E., Gipe, P., Beurskens, J., and Ottermo, F., "A historical review of vertical axis wind turbines rate 100 kW and above," Renewable and Sustainable Energy Reviews Vol. 105, 2019, pp. 1-13. https://doi.org/10.1016/j.rser.2018.12.022.
2. Tummala, A., Velamati, R.K., Sinha, D.K., Indraja, V. and Hari Krishna,V., "A review on small scale wind turbine," Renewable and Sustainable Energy Reviews, Vol. 56, 2016, pp, 1351-1371. http://dx.doi.org/10.1016/j.rser.2015.12.027.
3. Keisar, D., Eilan, B. and Greenblatt, D., "High pressure vertical axis wind pump," Journal of Fluids Engineering, Vol. 143, Issue 5, 2021, 051204 (9 pages). https://doi.org/10.1115/1.4049692.
4. Keisar, D., Freger, V. and Greenblatt, D., "Direct wind-powered vertical axis brackish water desalination system," Desalination, Vol. 570, 2024, pp. 117060. https://doi.org/10.1016/j.desal.2023.117060.
5. Miller, M.A., Duvvuri, S. and Hultmark, M., "Solidity effects on the performance of vertical- axis wind turbines," Flow, Vol. 1, E9, 2021. https://doi.org/10.1017/flo.2021.9.
6. Hui, I., Cain, B.E. and Dabiri, J.O., "Public receptiveness of vertical axis wind turbines," Energy Policy, Vol. 112, 2018, pp. 258-271. http://doi.org/10.1016/j.enpol.2017.10.028.
7. Migliore, P.G., "Comparison of NACA 6-series and 4-digit airfoils for Darrieus wind turbines. Journal of Energy, Vol. 7, No. 4, 1983, pp. 291-292. https://doi.org/10.2514/3.48083.
8. Ma, N., Lei, H., Han, Z., Zhou, D., Bao, Y., Zhang, K., Zhou, L. and Chen, C., "Airfoil optimization to improve power performance of a high-solidity vertical axis wind turbine at a moderate tip speed ratio," Energy, Vol. 150, 2018, pp. 236-252. https://doi.org/10.1016/j.energy.2018.02.115.
9. Baghdadi, M., Elkoush, S., Akle, B. and Elkhoury, M., "Dynamic shape optimization of a vertical-axis wind turbine via blade morphing technique," Renewable Energy, Vol. 154, 2020, pp. 239-251. https://doi.org/10.1016/j.renene.2020.03.015.
10. Zhao, Z., Wang, D., Wang, T., Shen, W., Liu, H. and Chen, M., "A review: Approaches for aerodynamic performance improvement of lift-type vertical axis wind turbine," Sustainable Energy Technologies and Assessments, Vol. 49, 2022, p.101789. https://doi.org/10.1016/j.seta.2021.101789.

11. Zhu, H., Hao, W., Li, C., Ding, Q. and Wu, B., "A critical study on passive flow control techniques for straight-bladed vertical axis wind turbine," Energy, Vol. 165, Part A, 2018, pp. 12-25. https://doi.org/10.1016/j.energy.2018.09.072.
12. Syawitri, T.P., Yao, Y., Yao, J. and Chandra, B., "A review on the use of passive flow control devices as performance enhancement of lift‐type vertical axis wind turbines," Wiley Interdisciplinary Reviews: Energy and Environment, Vol 11, No. 4, 2022, p.e435. https://doi.org/10.1002/wene.435.
13. Elkhoury, M., Kiwata, D. and Aoun, E., "Experimental and numerical investigation of a three-dimensional vertical-axis wind turbine with variable-pitch," Journal of Wind Engineering and Industrial Aerodynamics, Vol. 139, Apr 2015, pp. 111-123. http://dx.doi.org/10.1016/j.jweia.2015.01.004.
14. Sagharichi, A., Zamani, M. and Ghasemi, A., "Effect of solidity on the performance of variable-pitch vertical axis wind turbine. Energy," Vol. 161, 2018, pp. 753-775. https://doi.org/10.1016/j.energy.2018.07.160.
15. Sasson, B. and Greenblatt, D., "Effect of leading-edge slot blowing on a vertical axis wind turbine," AIAA Journal, Vol. 49, No. 9, 2011, pp. 1932-1942. http://doi.org/10.2514/1.J050851.
16. Greenblatt D. and Lautman, R., "Inboard/outboard plasma actuation on a vertical-axis wind turbine," Renewable Energy, Vol. 83, 2015, pp. 1147-1156. https://doi.org/10.1016/j.renene.2015.05.020.
17. Rezaeiha, A., Montazeri, H. and Blocken, B., "Active flow control for power enhancement of vertical axis wind turbines: Leading-edge slot suction," Energy, Vol. 189, 2019, p. 116131. https://doi.org/10.1016/j.energy.2019.116131.
18. Maeda, T., Kamada, Y., Murata, J., Shimizu, K., Ogasawara, T., Nakai, A. and Kasuya, T., "Effect of solidity on aerodynamic forces around straight-bladed vertical axis wind turbine by wind tunnel experiments (depending on number of blades)," Renewable Energy, Vol. 96, 2016, pp. 928-939. https://doi.org/10.1016/j.renene.2016.05.054.
19. Le Fouest, S. and Mulleners, K., "The dynamic stall dilemma for vertical-axis wind turbines," Renewable Energy, Vol. 198, 2022, pp. 505-520. https://doi.org/10.1016/j.renene.2022.07.071.
20. Greenblatt, D., Ben-Harav, A. and Mueller-Vahl, H., "Dynamic stall control on a vertical-axis wind turbine using plasma actuators," AIAA Journal, Vol. 52, No. 2, 2014, pp. 456-462. http://dx.doi.org/10.2514/1.J052776.

21. Müller-Vahl, H., Strangfeld, C., Nayeri, C.N., Paschereit, C.O. and Greenblatt, D., "Thick airfoil dynamic stall," in "Wind Energy – Impact of Turbulence," Eds. M. Hölling, J. Peinke and S. Ivanell, Springer, pp. 35-40, 2013. https://doi.org/10.1007/978-3-642-54696-9_6.
22. Medina, A., Ol, M.V., Greenblatt, D., Müller-Vahl, H. and Strangfeld, C., "High amplitude airfoil surging: complimentary wind and water tunnel experiments," AIAA Journal, Vol. 56, No. 4, 2018, pp. 1703-1709. http://doi.org/10.2514/1.J056408.
23. Müller-Vahl, H.F., Strangfeld, C., Nayeri, C.N., Paschereit, C.O. and Greenblatt, D., "Dynamic stall under combined pitching and surging," AIAA Journal, Vol. 58, No. 12, 2020, pp. 5134-5145. https://doi.org/10.2514/1.J059153.
24. Keisar, D., De Troyer, T. and Greenblatt, D., "Concept and operation of a wind turbine driven by dynamic stall," *AIAA Journal*, Vol. 58, No. 6, 2020, pp. 2370-2376. https://doi.org/10.2514/1.J059487.
25. Migliore, P. G., Wolfe, W. P., and Fanucci, J. B., "Flow Curvature Effects on Darrieus Turbine Blade Aerodynamics," Journal of Energy, Vol. 4, No. 2, 1980, pp. 49-55. https://doi.org/10.2514/3.62459.
26. Balduzzi, F., Bianchini, A., Maleci, R., Ferrara, G. and Ferrari, L., "Blade design criteria to compensate the flow curvature effects in H-Darrieus wind turbines," Journal of Turbomachinery, Vol. 137, No 1, p. 011006-1-10. https://doi.org/10.1115/1.4028245.
27. Bianchini, A., Balduzzi, F., Ferrara, G. and Ferrari, L., "Virtual incidence effect on rotating airfoils in Darrieus wind turbines," Energy Conversion and Management, Vol. 111, 2016, pp. 329-338. http://dx.doi.org/10.1016/j.enconman.2015.12.056.
28. Li, Q., Maeda, T., Kamada, Y., Murata, J., Shimizu, K., Ogasawara, T., Nakai, A. and Kasuya, T., "Effect of solidity on aerodynamic forces around straight-bladed vertical axis wind turbine by wind tunnel experiments," Renewable Energy, Vol 96, part A, Oct 2016, pp 928-939. http://dx.doi.org/10.1016/j.renene.2016.05.054.
29. Guo, Y., Li, X., Sun, L., Gao, Y., Gao, Z. and Chen, L., "Aerodynamic analysis of a step adjustment method for blade pitch of a VAWT," Journal of Wind Engineering and Industrial Aerodynamics, Vol. 188, 2019, pp. 90-101. https://doi.org/10.1016/j.jweia.2019.02.023.
30. Rezaeiha, A., Montazeri, H. and Blocken, B. "Towards optimal aerodynamic design of vertical axis wind turbines: Impact of solidity and number of blades," Energy Vol. 165, 2018, pp. 1129-1148. https://doi.org/10.1016/j.energy.2018.09.192.

31. Sutherland, H.J., Berg, D.E. and Ashwill, T.D., "A retrospective of VAWT technology," Sandia National Laboratories Report Sand2012-0304, 2012, pp. 1-64. https://doi.org/10.2172/1035336.
32. Zhu, H., Hao, W., Li, C. and Ding, Q., "Effect of flow-deflecting-gap blade on aerodynamic characteristic of vertical axis wind turbines," *Renewable Energy*, Vol. 158, 2020, pp. 370-387. https://doi.org/10.1016/j.renene.2020.05.092.
33. Mohamed, O.S., Ibrahim, A.A., Etman, A.K., Abdelfatah, A.A and Elbaz, A.M.R., "Numerical investigation of Darrieus wind turbine with slotted airfoil blades," Energy Conversion and Management: X, Vol. 5, Jan 2020, 100026. https://doi.org/10.1016/j.ecmx.2019.100026.
34. Ni, Z., Dhanak, M. and Su, T.C., "Improved performance of a slotted blade using a novel slot design," Journal of Wind Engineering and Industrial Aerodynamics, Vol. 189, Jun 2019, pp. 34-44. https://doi.org/10.1016/j.jweia.2019.03.018.
35. Belamadi, R., Djemili, A., Ilinca, A. and Mdouki, R., "Aerodynamic performance analysis of slotted airfoils for application to wind turbine blades," *Journal of Wind Engineering and Industrial Aerodynamics*, Vol. 151, 2016, pp.79-99. https://doi.org/10.1016/j.jweia.2016.01.011.
36. Klimas, P. C., "Vertical-Axis Wind Turbine Aerodynamic Performance Prediction Methods," Proceedings of the Vertical-Axis Wind Turbine (VAWT), Albuquerque, NM, April 1980, pp. 215-232.
37. Paraschivoiu I., "Double-multiple streamtube model for studying vertical-axis wind turbines," AIAA Journal of Propulsion, Vol. 4, No. 4, 1987, pp. 370-377.
38. Koss, D., Steinbuch, M. and Shepshlovich, M., "Development of two-element NLF airfoils for long endurance flight," AIAA Paper No. 1997-514, 35th Aerospace Sciences Meeting and Exhibit, Jan 1997. https://doi.org/10.2514/6.1997-514.
39. Keisar, D., Arava, I. and Greenblatt, D., "Dynamic-Stall-Driven Vertical Axis Wind Turbine: An Experimental Study, December, 2023. https://doi.org/10.13140/RG.2.2.19205.73441.
40. Greenblatt, D., "Unsteady low-speed wind tunnels," AIAA Journal, Vol. 54, No. 6, June 2016, pp. 1817-1830. https://doi.org/10.2514/1.J054590.
41. Kinsey, T. and Dumas, G., "Impact of Channel blockage on the performance of axial and cross- flow hydrokinetic turbines," Renewable Energy, Vol. 103, 2017, pp 239-254. https://doi.org/10.1016/j.renene.2016.11.021.

42. Carmichael, B.H., "Low Reynolds number airfoil survey," Volume 1, NASA-CR-165803-VOL-1, 1981. https://ntrs.nasa.gov/citations/19820006186.
43. Anderson, J.D., "Introduction to Flight," 8th Edition, Chapter 6, McGraw-Hill, New York, 2016.
44. Sheldahl, R.E. and Klimas, P.C., "Aerodynamic characteristics of seven symmetrical airfoil sections through 180-degree angle-of-attack for use in aerodynamic analysis of vertical axis wind turbines," Sandia National Laboratories, Energy Report SAND80-2114, March 1981.
45. Selig, M.S. and Guglielmo, J. J., "High-lift low Reynolds number airfoil design," AIAA Journal of Aircraft, Vol. 34, No. 1, 1997. https://doi.org/10.2514/2.2137.
46. Liebeck, R.H., "Design of subsonic airfoils for high lift," AIAA Journal of Aircraft, Vol. 15, No. 9, 1978. https://doi.org/10.2514/3.58406.
47. Steinbuch, M., Marcus. B. and Shepshelovich, M., "Development of UAV wing- subsonic designs," AIAA Paper No. 2003-603, 41st Aerospace Sciences Meeting and Exhibit, Jan 2003. https://doi.org//10.2514/6.2003-603.
48. Abdullah, M.A., Yatim, A.H.M., Tan, C.W. and Saidur, R., "A review of maximum power point tracking algorithms for wind energy systems," Renewable and Sustainable Energy Reviews, Vol. 16, Vol. 5, 2012, pp. 3220-3227. https://doi.org/10.1016/j.rser.2012.02.016.